Investigation on the characterization and modelling of Fracture Process Zone behavior in Concrete Beams subjected to Three-Point Loading Tests

H. S. Vishwanatha
Department of Civil Engineering, M.E.I Polytechnic; Department of Technical Education, Bangalore, Karnataka, India
hs_vish@yahoo.co.in

S. Muralidhara
Department of Civil Engineering, B.M.S. College of Engineering; Vishveshwarya Technical University, Bangalore, Karnataka, India
murali.civ@bmsce.ac.in

B. K. Raghu Prasad
Department of Civil Engineering, Indian Institute of Science, Bangalore, Karnataka, India
bkriisc@gmail.com

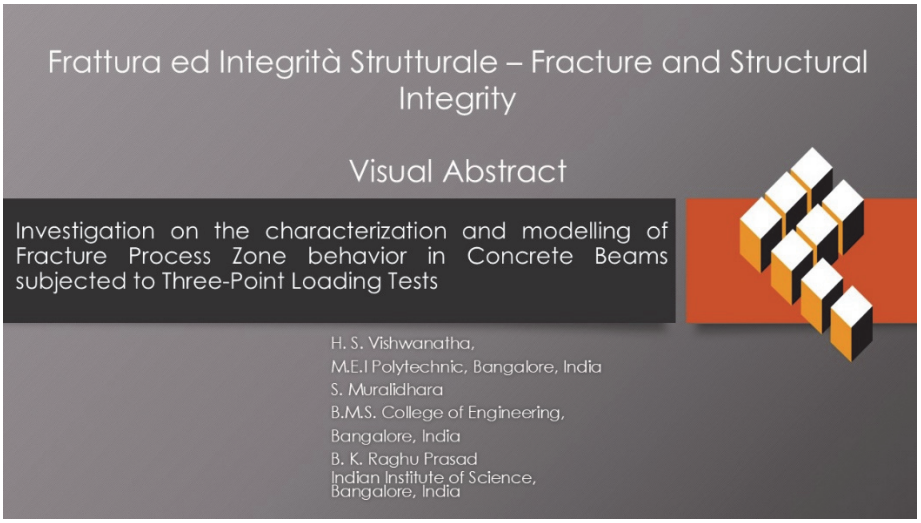

Citation: Vishwanatha, H., Murlidhara, S., Raghu Prasad, B. Investigation on the characterization and modelling of Fracture Process Zone behavior in Concrete Beams subjected to Three-Point Loading Tests, Fracture and Structural Integrity, 72 (2025) 80-101.

Received: 26.12.2024
Accepted: 31.01.2025
Online first: 06.02.2025
Published: 01.04.2025

KEYWORDS. Coarse aggregate, Fracture process zone, Load-deflection, Interfacial Transition Zone.

INTRODUCTION

The fracture process zone (FPZ) in concrete is a critical region where micro-cracks develop and coalesce, eventually leading to macroscopic crack propagation. The size and characteristics of the FPZ are influenced by the material heterogeneity and the applied loading conditions. In three-phase concrete materials with pre-existing cracks, three distinct crack propagation paths can typically be identified:

- ✓ Cracks within Cement Mortar: These cracks propagate through the cement mortar phase of the material.
- ✓ Cracks along the Mortar-Aggregate Interface: In this situation, cracks propagate along the interface between the cement mortar and the aggregate particles.
- ✓ Cracks Kinking into the Interface: These cracks deviate from their initial path and intersect the mortar-aggregate interface at an oblique angle.

Each of these propagation paths may have its own criterion governing crack growth. Determining the direction of crack initiation or extension involves applying the appropriate crack propagation criterion for each case. This process enables the prediction of crack behaviour and its interaction with the material phases in three-phase concrete systems.

Researchers have extensively studied the FPZ to understand its role in the overall fracture behavior of concrete. Digital image correlation (DIC) and electronic speckle pattern interferometry (ESPI) have enabled detailed observations of the FPZ, revealing intricate crack patterns and stress distributions within this zone [1,2]. The present study focuses on a detailed analysis of the FPZ and its evaluation for beams ranging from small to very large sizes (75 mm to 1000 mm).

MODEL GENERATION

The mortar, composed of fine aggregates and cement, typically acts as the composite matrix. Aggregates, the strongest constituents of concrete, account for approximately 75% of its volume, with coarse aggregates making up 40–50% based on the specific design mix [4]. The coarse aggregates embedded in the mortar matrix are the primary reinforcing elements. They significantly influence the fracture behavior by bridging cracks, altering the FPZ characteristics, and increasing the materials resistance to crack propagation. The interfacial transition zone (ITZ), which generally forms around the aggregates, is often considered the weakest region [3].

The key steps in parameterized modeling [3] for constructing a two-dimensional concrete model involve determining the total area occupied by aggregates in accordance with a specified aggregate gradation. Particles larger than 4.75 mm are categorized as coarse aggregates, which are distributed within the concrete to act as the reinforcing matrix phase. Aggregates of various sizes are created and randomly arranged within the defined area.

In this study, spherical aggregates (appearing circular in 2D models) were randomly distributed. Using the Monte Carlo method, aggregates were generated and randomly placed within the specimen's specified dimensions and aggregate fraction. A Python script was utilized, incorporating a loop with check-and-reject functions to ensure proper placement. Small gaps were intentionally left for the cement matrix during the distribution process, and the number of iterations was predefined. The fig.1(a) shows flow chart adopted for distribution of different sizes of coarse aggregates. An aggregate volume fraction of 40% was used in this analysis. Fig. 1(b) shows typical aggregate distribution after executing Python script. During the simulation, the aggregate positions were varied in each iteration. Three iterations for each specimen size were carried out to represent the randomness of aggregate distribution in three trials.

In this study, a Python script was imported into Abaqus for conducting the analysis. The gematrical properties as per Tab. 1 adopted and the materials assigned as per the Tab. 2. The boundary conditions provided to suit simply supported beam with central point load. A displacement load was applied, consisting of 10,000 load steps with a constant load increment. This loading procedure allowed for the crack to penetrate through the entire beam height, providing a detailed understanding of the fracture process in concrete. The flowchart adopted for model generation and analysis is depicted in fig. 3.

Due to the model's inherent randomness in aggregate distribution, achieving a well-structured mesh presents challenges. Notably, issues arise with the interfacial mesh between aggregates and mortar. These issues encompass smaller mesh areas, higher mesh density, and non-uniform mesh sizes compared to other regions. These mesh-related complications hinder the convergence of the realistic aggregate model, largely due to mesh distortion.

In essence, crack propagation and fracturing in concrete numerical simulations are intricately tied to mesh generation. For finite element simulations where the cohesive crack paths are not known in advance, rather fine levels of discretization must be used to reduce the dependence of the cohesive crack paths on the mesh size. However, reducing the element size leads to an increase in computational cost, so a balance between computational cost and accuracy must be established. To this end, a mesh convergence study is performed in this work in terms of the mean stress–strain curve and the final fracture crack paths to find an optimal mesh size.

This study examined five different mesh sizes (0.5 mm, 1 mm, 2 mm, and 4 mm). A mesoscale concrete model size of 150mm×150mm×50mm with coarse aggregate volume fraction of 40% was utilized. The Material properties as per Tab. 2 adopted. Following discretization, all specimens underwent with a uniform displacement of 0.15 mm in the x-direction. The mean stress–strain curves for each mesoscale specimen are presented in fig. 2. Mean stress was determined by dividing the total reaction forces at the left edge nodes by the specimen's length at each step frame.

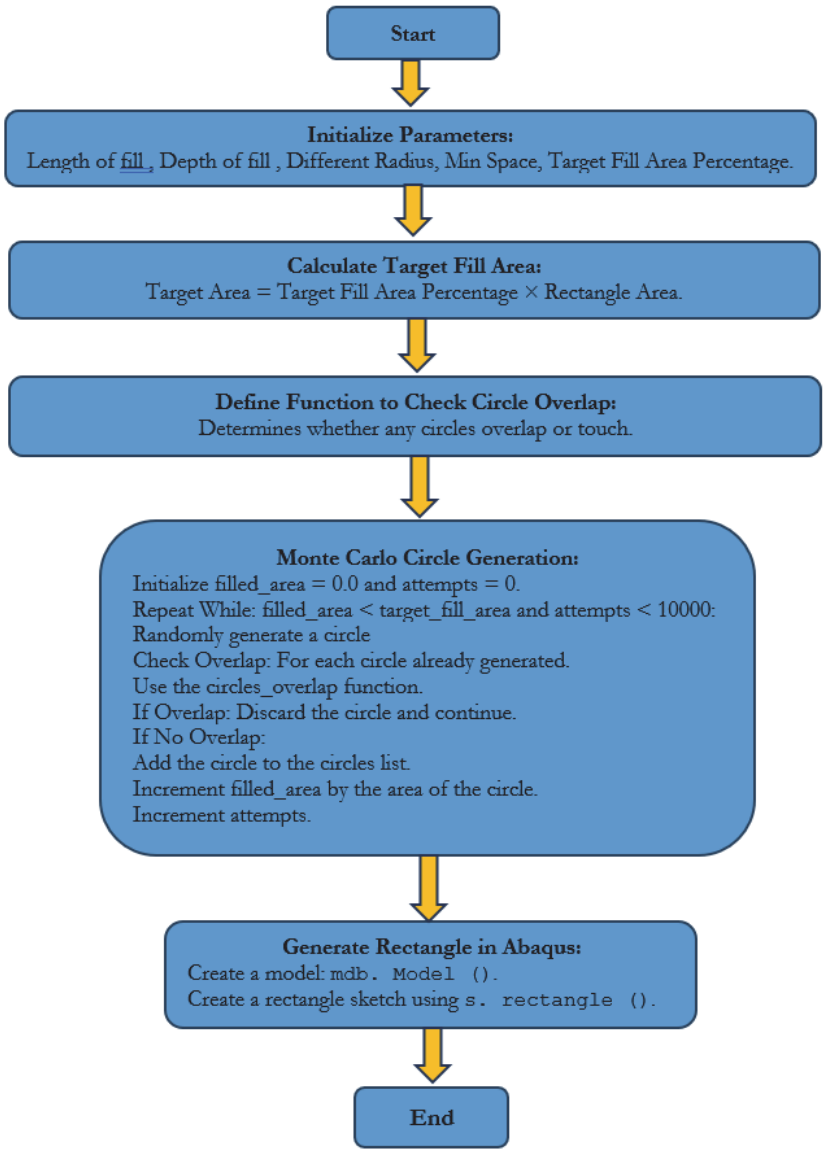

Figure 1(a): Flow chart showing generation of aggregates using Python script.

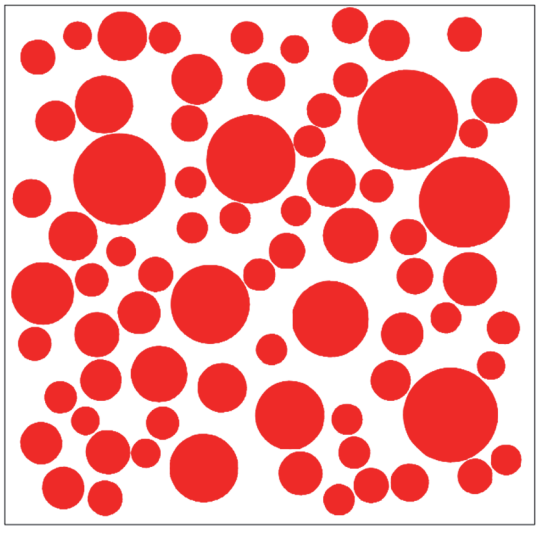

Figure 1(b): Aggregates distribution.

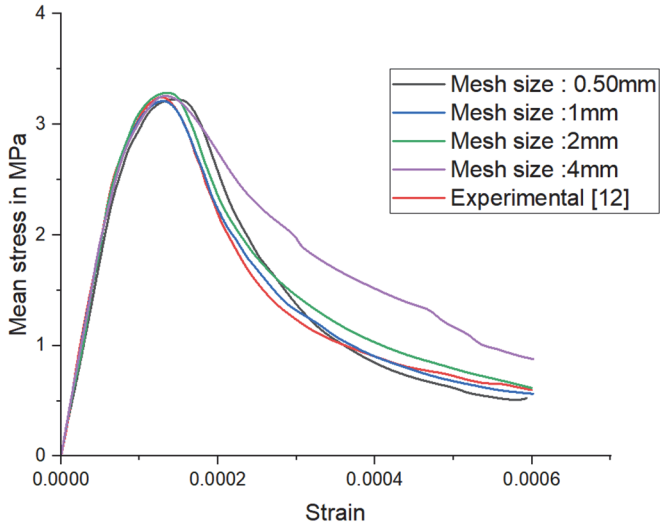

Figure 2: Mean stress–strain curve for a concrete sample shown in with different levels of discretization.

The stress–strain curves and macrocrack patterns for specimens with mesh sizes of 1 mm and 2 mm showed strong agreement with the experimental results obtained from [12]. However, meshes finer than 1 mm resulted in poorly meshed regions, while coarser meshes caused element distortion and unfavorable mesh angles. Considering that mesh sizes between 1 mm and 2 mm are widely employed in prior studies [5], this research adopted mesh sizes within this range based on a mesh sensitivity analysis.

The convergence study underscored the importance of fracture paths in selecting an appropriate mesh size in addition to stress–strain curves. Although larger meshes may provide similar stress–strain results, they often lead to significantly different fracture paths. Conversely, smaller meshes yielded consistent fracture paths and stress–strain curves, but further reduction drastically increased computational demands.

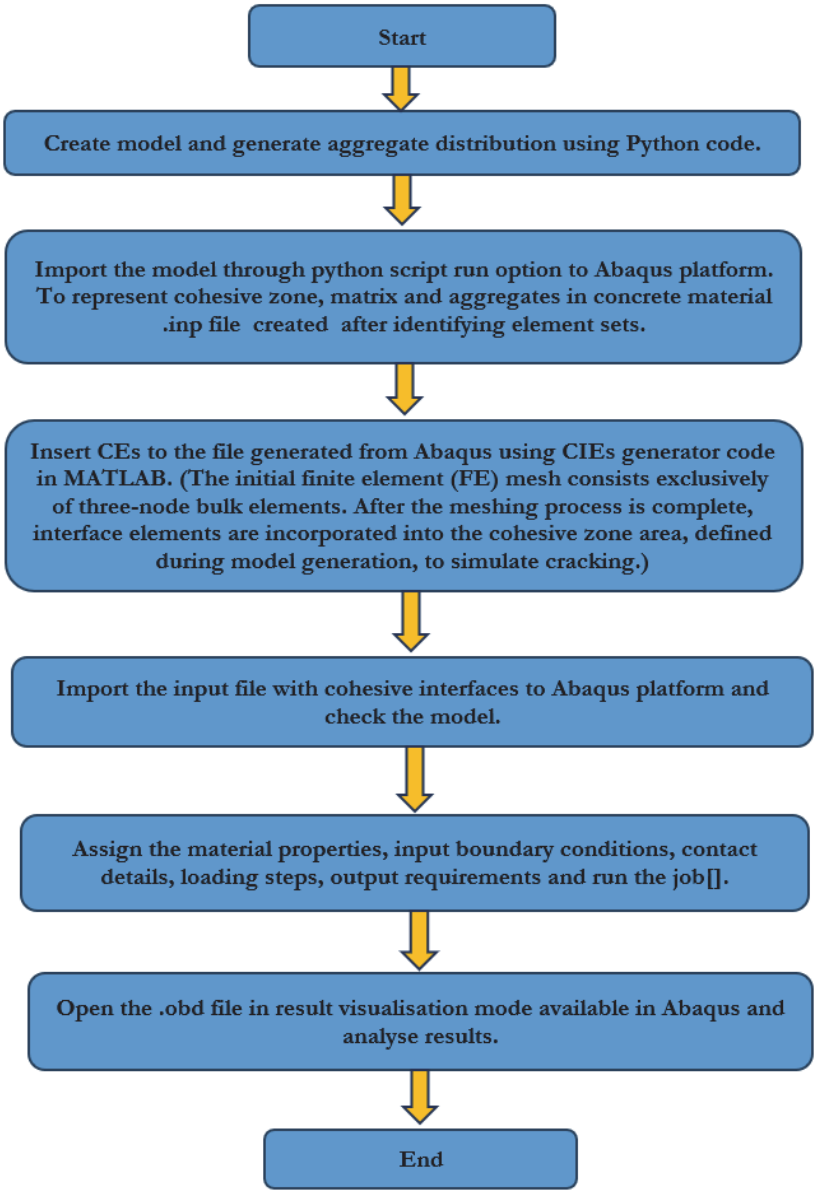

Figure 3: Flow chart illustrating methodology.

GEOMETRICAL PROPERTIES OF BEAMS

Tab. 1 shows the geometrical properties of the beams adopted in the present study. The beams were grouped into five beams. Each type of beam was analysed with three different configurations of coarse aggregate (CA). In the nomenclature employed: B-SB75, the first letter B represent beam series, SB represents small beam and last digit

represents depth or size of beam. The MB stands for medium beam, LB for large beam, VB for very large beam & HB for huge beam.

Beam ID	Depth of beam (D) mm	Breath of beam (b) mm	Length of the beam (L) mm	Span (S) mm	Central part of beam (S_0) mm	Notch to depth ratio $\alpha_0=a_0/D$	Depth of notch (a_0) mm	S/D
B-SB75	75	150	250	225	50	0.25	18.75	3
B-MB150	150	150	550	450	100		37.5	
B-LB250	250	150	1000	750	150		62.5	
B-VB500	500	150	2000	1500	300		125	
B-HB1000	1000	150	4000	3000	600		250	

Table 1: Geometrical properties of the beams.

To save computational time and memory, the central part of the beam is modeled as a heterogeneous section with a fine mesh, while the side parts are modeled as homogeneous sections. This approach is illustrated in Fig.4,5,6. The heterogeneous section in the central part allows for a detailed representation of the microstructure where stress and strain concentrations are expected to be higher, whereas the homogeneous side sections reduce computational demands without significantly affecting the accuracy of the overall model. This method strikes a balance between accuracy and computational efficiency, ensuring that the key areas of interest are accurately simulated.

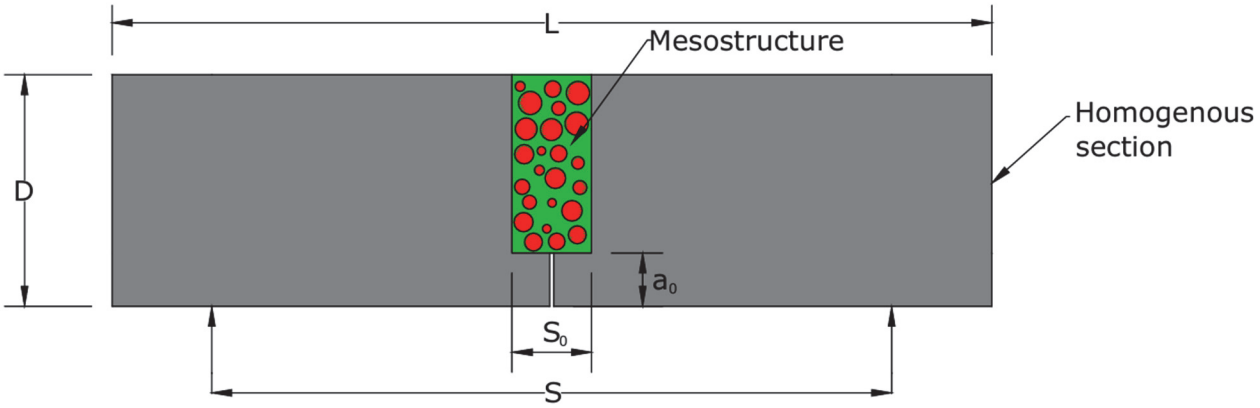

Figure 4: Spherical shape aggregates (SSA-Model).

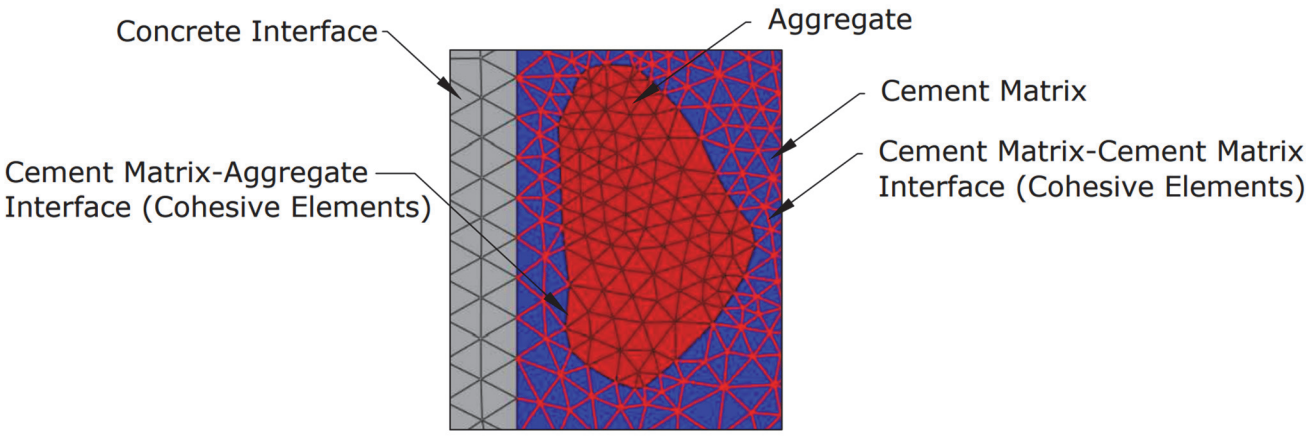

Figure 5: Interfaces in microstructure.

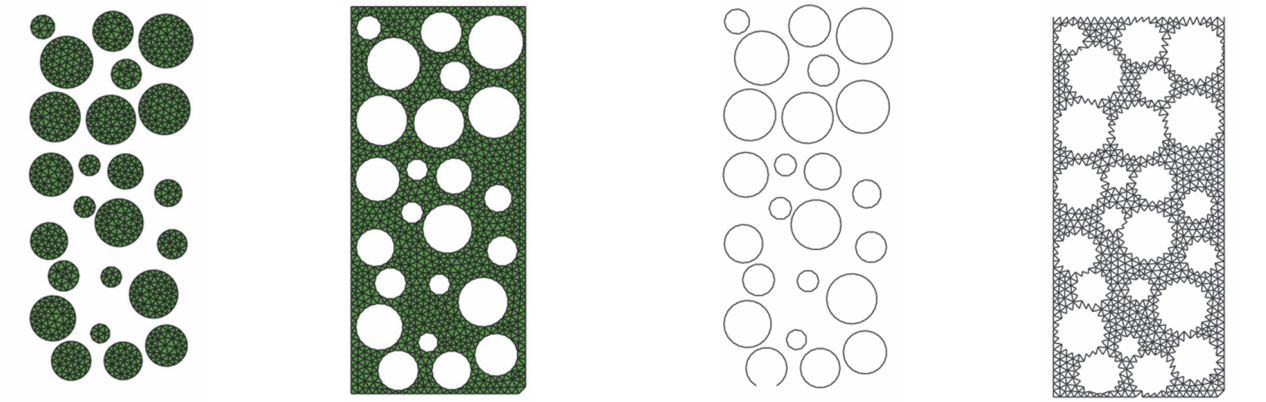

(a)Aggregates (b)Matrix (c) Cohesive elements at ITZ (d) Cohesive elements at Cement matrix

Figure 6: Heterogeneous region for SSA models.

MATERIAL PROPERTIES

In the FE model, the solid elements that represent the mortar and aggregates are assumed to behave in a linear elastic manner. Most of the deformation occurring between two solid elements is absorbed by the cohesive elements. The solid elements only deform when the cohesive elements are within their linear elastic range. Due to the very high initial stiffness of the cohesive elements, they experience negligible deformation within this range, resulting in minimal deformation of the solid elements.

Elements	Parameter	Density (kg/m^3)	Young's Modulus, E (MPa)	Poisson's ratio, υ	Traction-Separation Law		
					Elastic Stiffness (MPa)	Cohesive strength (MPa) (Damage initiation)	Fracture energy (N/mm)
Bulk	Aggregate	2800	47200	0.2	-	-	-
	Cement matrix	2400	29200	0.2	-	-	-
	Homogeneous beam part	2400	36100	0.2	-	-	-
Cohesive	CIEs	2400	-	-	10^6	3.5	0.168
	ITZs	2300	-	-	10^6	2.4	0.115

Table 2: Material properties adopted in FE analysis for concrete beam [6, 7].

VALIDATION OF THE MODEL

The effect of shapes of aggregate particles investigated with beams of same geometry and material parameters with spherical shape. Three point bending test conducted and load-deflection curves plotted. Fig.7 shows the results of 10 beams with spherical aggregates takes average peak load 7.10kN. The maximum discrepancy of the peak load between the experimental and numerical values is 6.5 % for the Spherical shape aggregates.

From the final crack distribution and crack development process, as shown in Fig. 8, it is evident that the macroscopic crack initiates near the notch tip, where stress concentration is highest due to the applied boundary conditions. The crack propagates upward, interacting with the mortar and aggregates, ultimately pointing toward the loading point. The figure illustrates the progression of the crack through the heterogeneous section, influenced by the relative positions of aggregates and the stress field distribution.

The crack of the spherical aggregate model begins developing in small aggregates and mortar and reaches aggregate 'a' as shown in Fig.8, where the development of cracks is blocked and continues to develop upward along the boundary of aggregate 'a'.

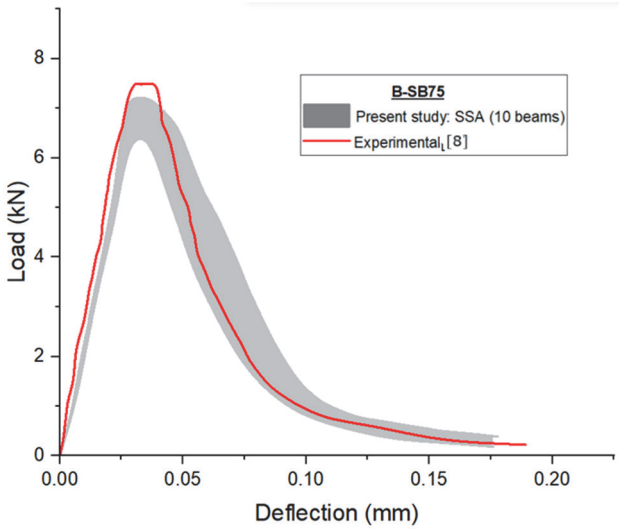

Figure 7: Load-deflection curves for B-SB75.

The same phenomenon, known as the aggregate blocking effect, is seen for aggregates b-c-d-e-f in Fig.8. Therefore, it can be concluded that the aggregate geometry has the effect of blocking and guiding the crack, while the blocking effect tends to occur in the spherical aggregate model. The results indicated that the geometric properties of aggregates have both blocking and guiding effects on crack development. The present study focuses on medium-strength concrete, where the crack propagation predominantly occurs along the weak interfacial transition zone (ITZ) due to the relatively lower strength of the matrix compared to the aggregate. However, in high-strength concrete, the ITZ is significantly strengthened due to the reduced porosity and improved bonding between the matrix and the aggregate. As a result, the crack is more likely to propagate through the aggregate itself, destroying it and altering its trajectory.

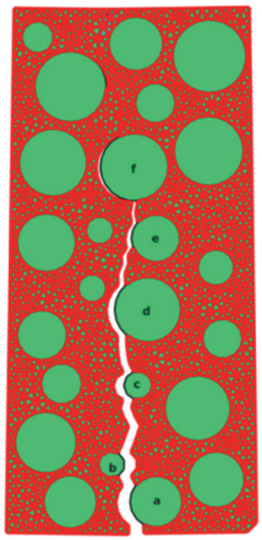

Figure 8: Crack Propagation under TPB test at heterogeneous section (Central part of beam).

IDENTIFICATION OF LOADING STEPS

To investigate crack propagation in the fracture procedure, ten steps were selected, as shown in Fig. 9. Based on the results of analysis, the load deflection curve of the TPB with the notch-to-depth ratio of 0.25 plotted, and the results are shown in Fig.9. In Fig. 9, P_1 point selected after initial crack load. At P_1, cracking starts at the notch tip. As cracking progresses, the load in P_2 approaches the maximum load with a less steep slope than in P_1. The load at P_2 reaches

its peak value and from this point onwards leads to unstable fracture, which is reflected in areas P_3 to P_{10} of the load–displacement curve.

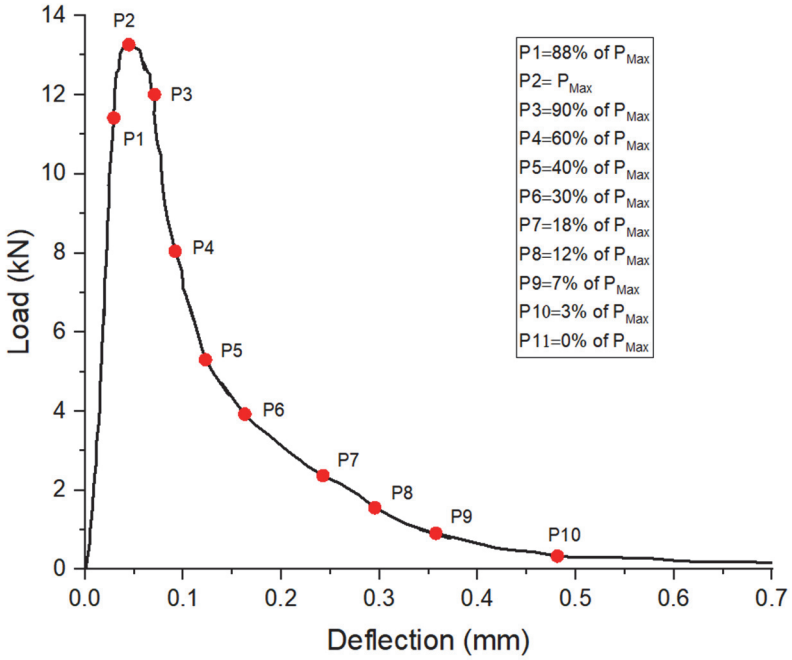

Figure 9: Typical Load- Displacement curve showing different loading steps to evaluate FPZ for B-MB150

ANALYSIS OF LOAD-CMOD AND LOAD-CTOD PLOTS

Fig. 10 depicts the load-crack mouth opening displacement (P-CMOD) and load-crack tip opening displacement (P-CTOD) curves for five concrete beam sizes (B-SB-75, B-MB-150, B-LB-250, B-VB-500, and B-HB-1000) as determined from the analysis. The P-CMOD curve exhibits an approximately linear trend up to the peak load, transitions to a nonlinear phase near the peak, and then demonstrates distinct softening behavior beyond the peak load. Furthermore, the results indicate that the peak load increases with the size of the beams. In Fig.10, "PC" denotes the loading step at which the fracture process zone reaches its maximum length.

To highlight the differences between CMOD and CTOD, both values from the same beam are shown in Fig.10. It is evident that the shape of the P-CTOD curve closely resembles that of the P-CMOD curve, though the P-CTOD values are consistently smaller than the corresponding CMOD values under identical conditions.

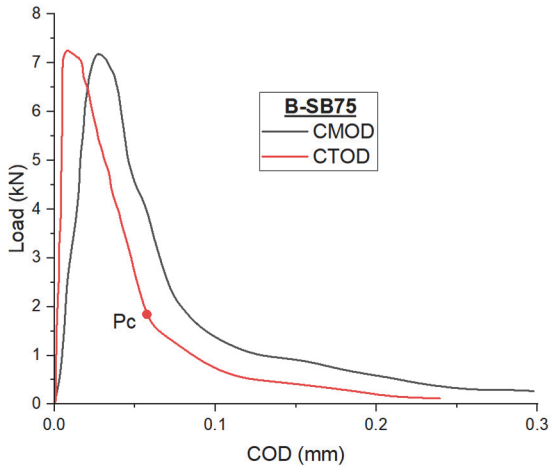

(a) B-SB75

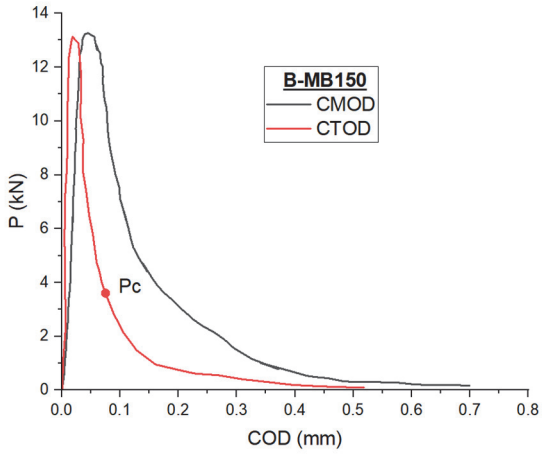

(b) B-MB150

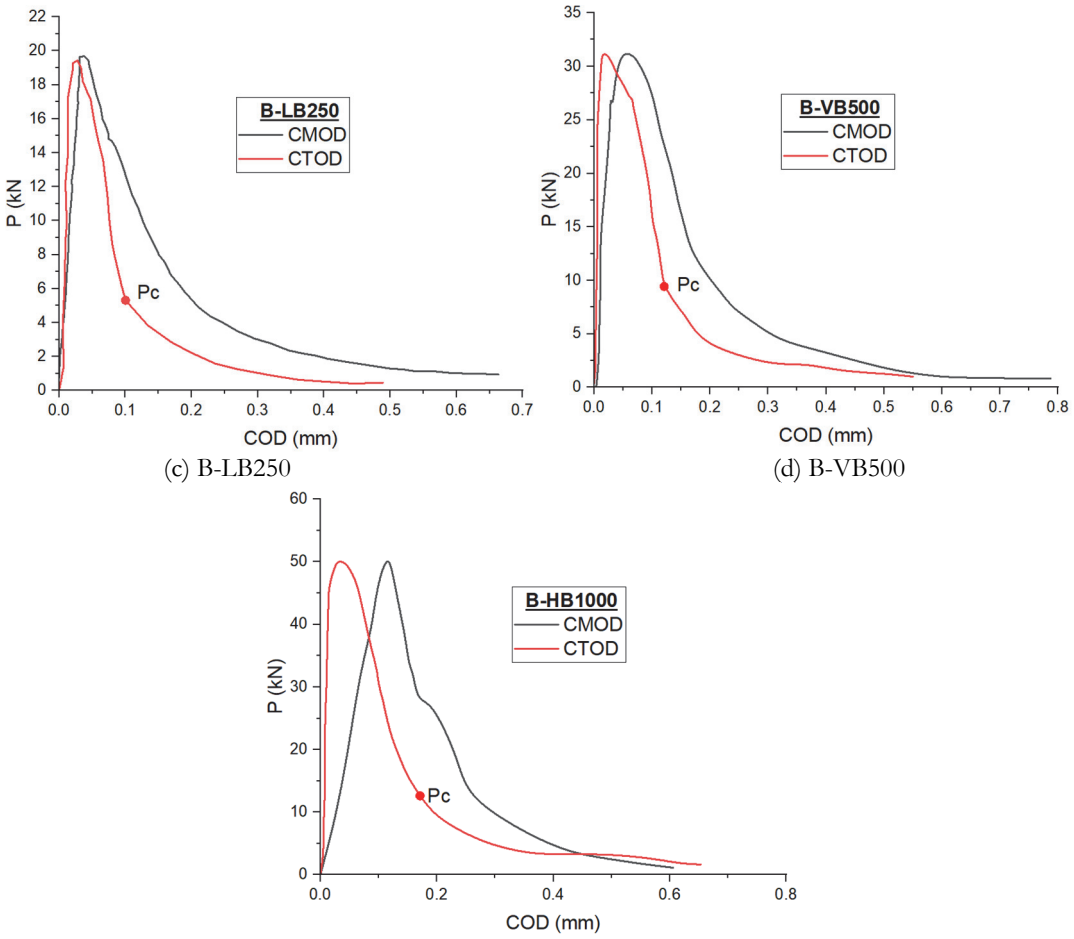

(c) B-LB250 (d) B-VB500

(e) B-HB1000

Figure 10: Load-CMOD and Load-CTOD plots.

As shown in Fig.11, no microcracks are observed in the concrete material when the load is below 40% of the peak load. During this phase, the P-CMOD curve remains nearly linear, signifying a linear elastic stage with only a slight difference between CMOD and CTOD. Once the load exceeds the proportionality limit, the difference between CMOD and CTOD progressively increases with the applied load. As crack propagation occurs, the rotation angle between the crack mouth and crack tip increases, further amplifying the variation in COD values.

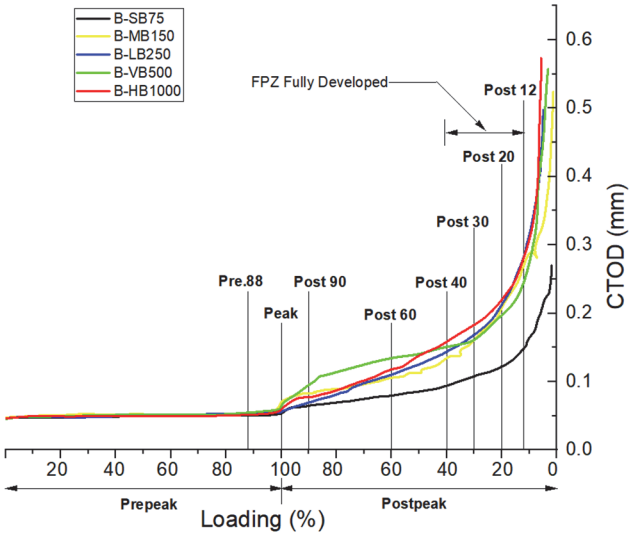

Figure 11: CTOD versus Percentage of Peak loading during pre peak and post peak.

EVALUATION OF FRACTURE PROCESS LENGTH

As shown in Fig. 12, the FPZ consists of a main crack and numerous secondary cracks. The main crack begins above the notch due to stress concentration at the notch tip and propagates upward due to bending. The secondary cracks primarily initiate and propagate through the weak interfacial transition zones (ITZs) along the boundaries of the strong aggregate particles. The main crack extends by bridging the interfacial micro-cracks that form around adjacent aggregates.

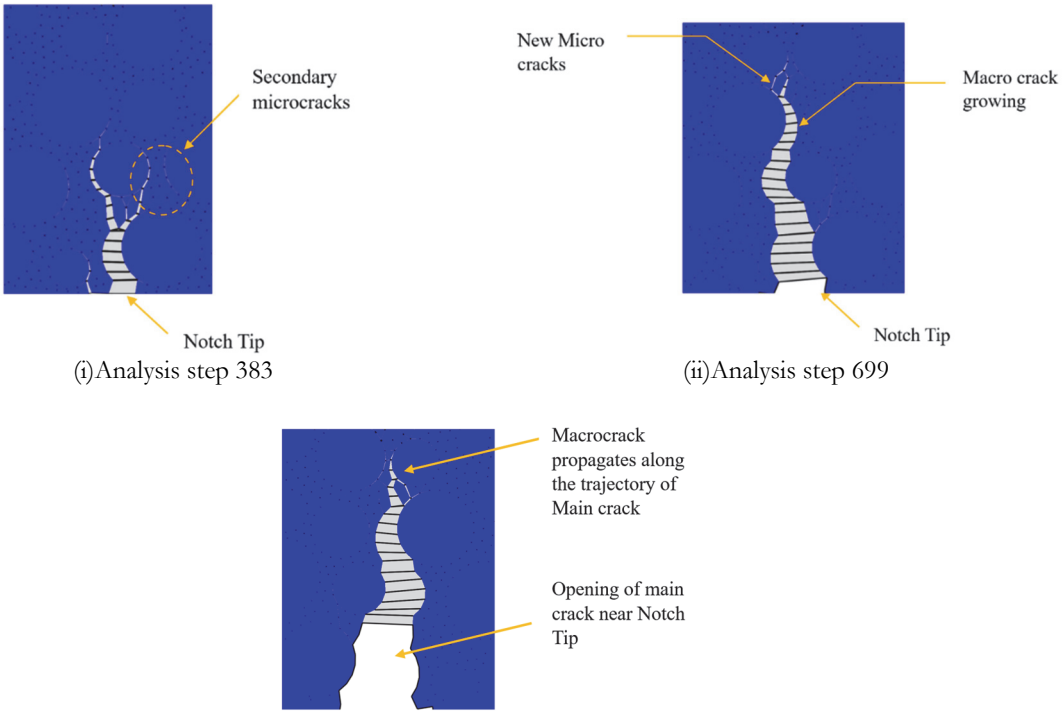

Figure 12: Development of cracks at interfaces.

During the growth of the main crack, many new cracks appear while some earlier-formed cracks cease to grow. The evolution path of the FPZ is highly irregular due to the random spatial distribution of aggregate particles with weak ITZs. The FPZ forms before the load reaches its maximum value and can expand significantly around the peak load. After the peak load, the FPZ continues to extend upward with the appearance of many new cracks, while the main crack forms and propagates. Since the extension of the FPZ is generally measured from the stress-free crack mouth (w_0) to the crack tip, the length of the FPZ may gradually decrease during the post-peak stage. This process is illustrated in Fig. 13. The findings of this study regarding the development mechanism of cracks in concrete align well with experimental observations using DIC, X-ray, CT, and AE techniques [9-13].

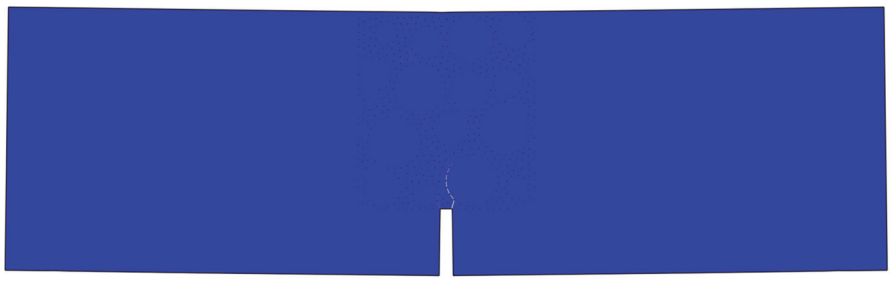

(i) At P_1

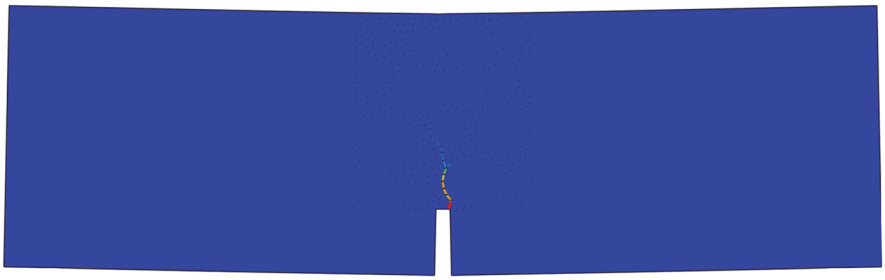

(ii) At P_2

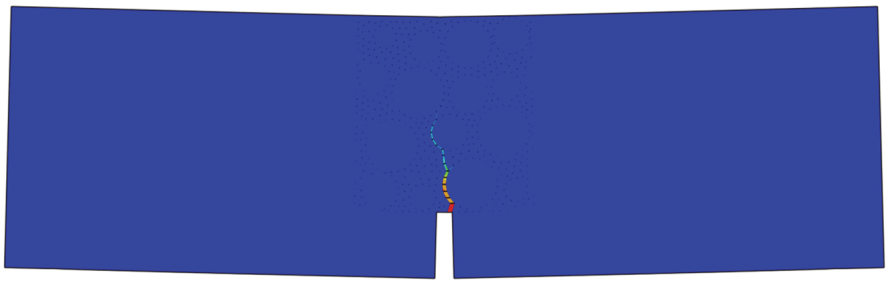

(iii) At P_3

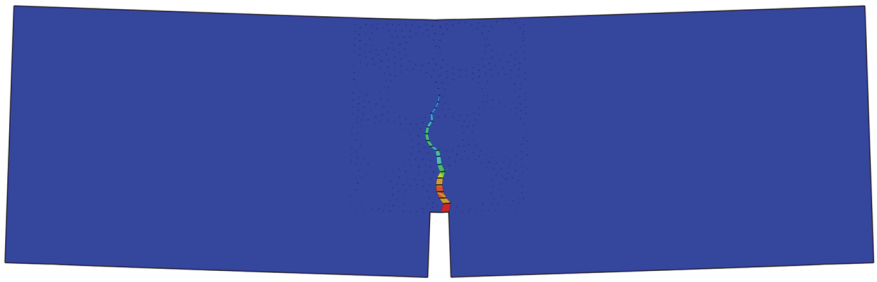

(iv) At P_4

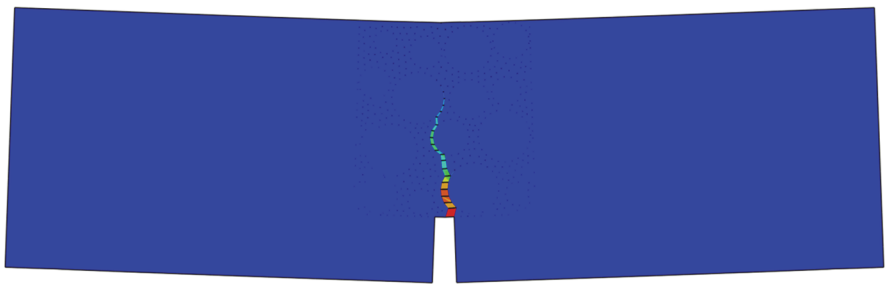

(v) At P_5

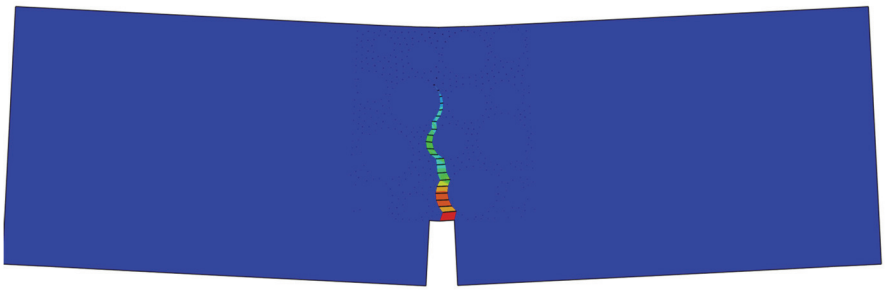

(vi) At P_6

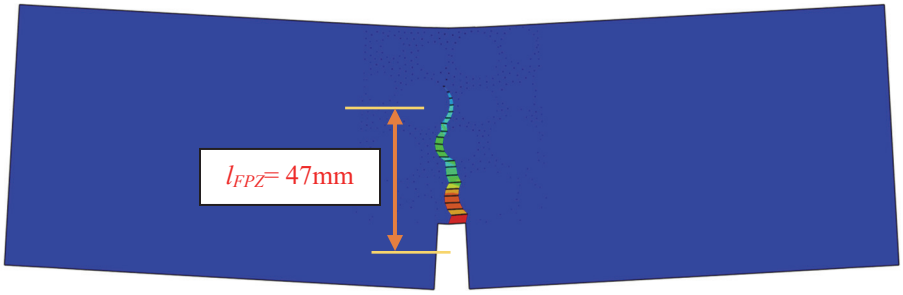

(vii) At P_C

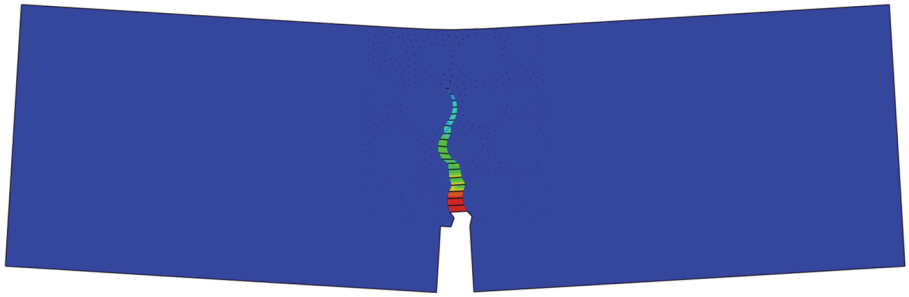

(viii) At P_7

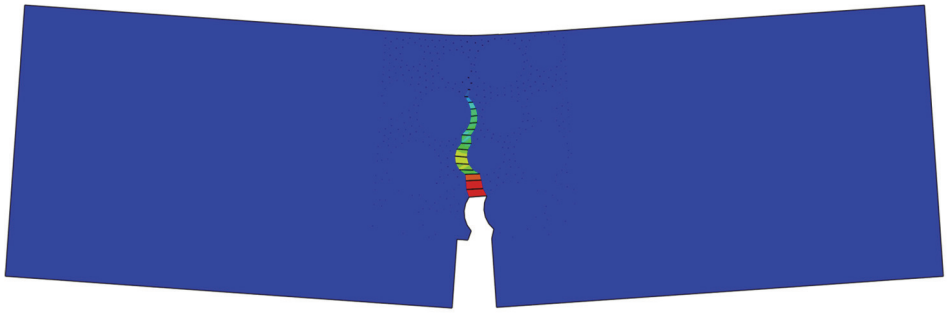

(ix) At P_8

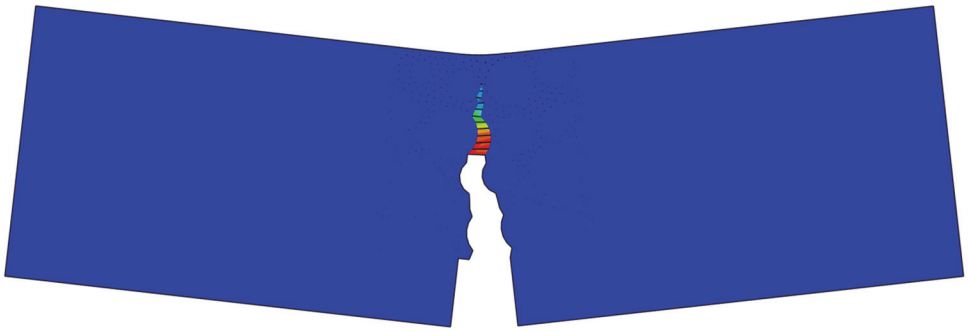

(x) At P_9

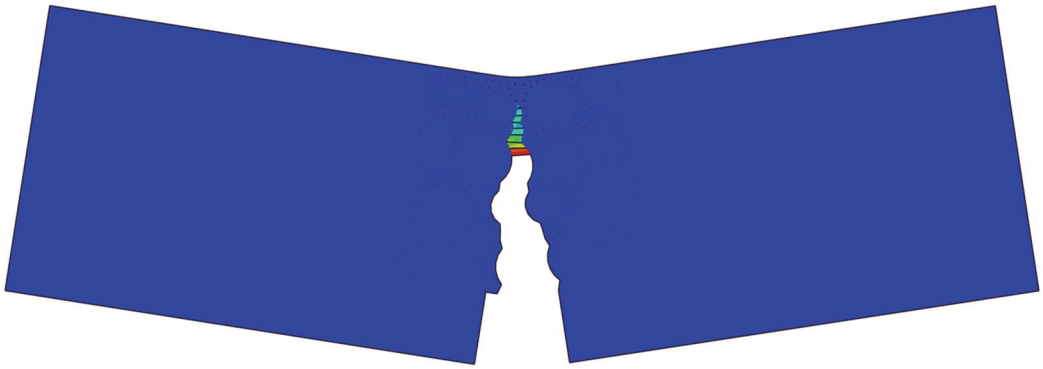

(xi) At P_{10}

Figure 13: Evaluation of Fracture Process Zone for B-SB75.

VARIATION OF FPZ LENGTH

The precise measurement of the fracture process zone (FPZ) is crucial for accurately predicting the fracture behavior of concrete. In this study, the FPZ length (l_{FPZ})was observed to investigate its changes during crack growth.

The critical crack tip opening displacement or Stress-free Crack opening displacement (w_0) is a measure of the displacement at the crack tip when the material reaches a critical state before rapid crack propagation.

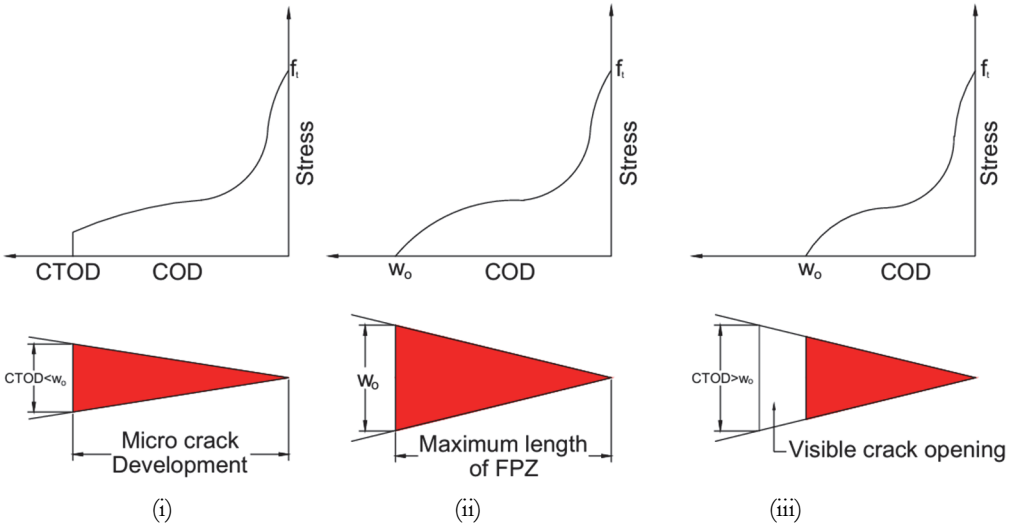

Figure 14: Development of fracture process zone length

At the initial loading stage (Refer Fig.14(i)), the crack tip opening displacement (CTOD) at the tip of the macrocrack is smaller than the w_0 (CTOD $\leq w_0$). With the process of loading, the CTOD gradually increases. When the it reaches critical value, maximum length of FPZ developed near notch area (Refer Fig.14(ii)). During post peak loading stage crack tip opens with visible crack as shown in Fig. 14(iii). The stages of complete fracture process depicted in Fig.14.

The ligament length (D-a_0) is the portion of the uncracked cross-section between the notch tip and the opposite edge of the beam or specimen. The ligament length determines the region available for the formation and development of the FPZ, where micro-cracking, aggregate bridging, and energy dissipation occur. A longer ligament length provides more material to resist crack propagation, leading to a larger FPZ. Ligament length directly affects the amount of fracture energy available for crack propagation. A shorter ligament reduces the capacity for energy dissipation in the FPZ, often leading to more brittle fracture behavior, whereas a longer ligament supports more stable crack growth.

For B-SB75, fracture process under various loading steps depicted in Tab. 3. At loading step P_1, a FPZ is observed forming ahead of the notch tip. The FPZ length measures 4.75mm, which is 0.085 times the ligament length (D-a_0=75-19=56mm). The crack tip opening displacement (w) is measured at 4.88μm.

As loading progresses to P_2 (the peak load), the FPZ length (l_{FPZ}) extends to 0.135 times the ligament length, with a w of 7.56µm. By loading step P_5, the l_{FPZ} increases to 0.698 times the ligament length, with a w of 49.65µm, resulting in the FPZ appearing as an irregular band. At loading point P_6, with a w of 51.25µm, the l_{FPZ} equal to 45.83 mm, 0.85 times the ligament length. When loading step P_7 reached, the l_{FPZ} becomes 35mm. Therefore it is observed that maximum l_{FPZ} developed between P_6 and P_7 loading steps.

From the visualization technique available in Abaqus CAE, the exact point P_C at which the crack tip opens up which is called Stress-free Crack opening displacement (w_0) could be noted. At that load the value of l_{FPZ}=47.5mm and w_0=52.67 µm. P_C is observed to be 26% of P_{Max} (Tab. 3). Further examination of the FPZ's variation, depicted in Fig.13, reveals that at Loading steps P_8, P_9, and P_{10}, the w exceeds w_0, leading to the formation of a new traction-free crack ahead of the notch tip. Interestingly, despite the crack tip advancing by 113.1µm and 150.7µm at loading steps P_8 and P_9, respectively, the FPZ length diminishes by 22.9mm and 17.5mm, respectively. Fig.15 shows fracture process zone at heterogenous section at P_3, P_C and P_7 for B-SB75 extracted from analysis results.

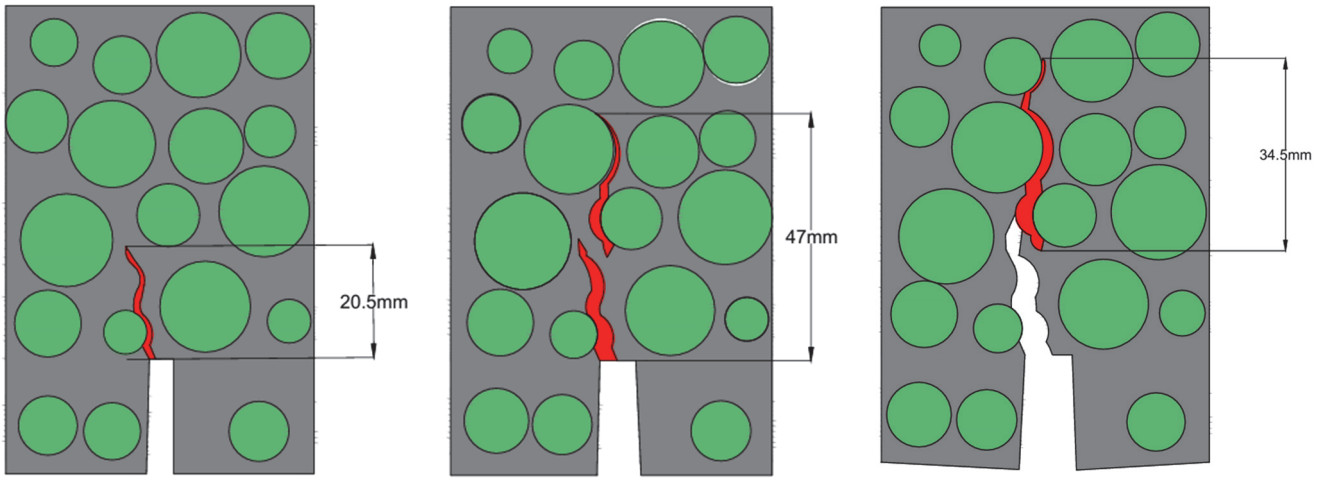

(i) At P_3 (ii) At P_C (iii) At P_7

Figure 15: Fracture process zone for B-SB75.

The final macrocrack trajectory in B-SB75, shown in Fig.16(iii), aligns well with the propagation path of the FPZ determined by the DIC method [9] and AE method [11] in Fig.15 (i,ii).

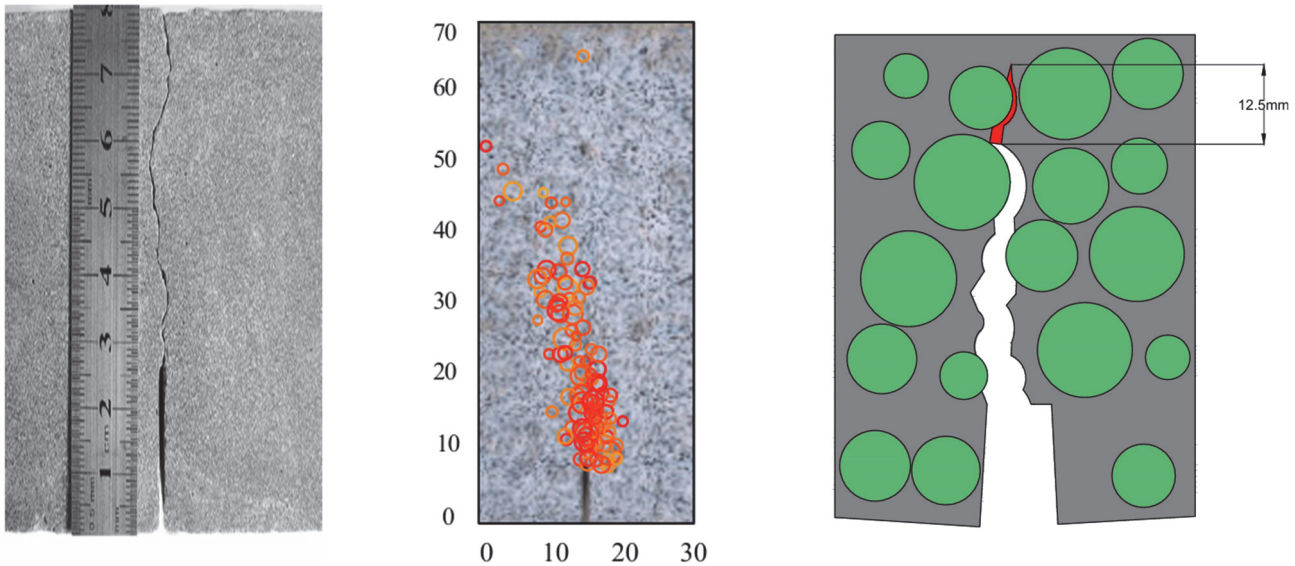

(i)The final crack trajectory [9]. (ii) The location of AE events in FPZ [11]. (iii) At loading step P_{10} (present study).

Figure 16: Propagation path of the FPZ

Loading steps	Pre-Peak	Peak	Post Peak								
	P_1 (88% of P_{Max})	P_2 (P_{Max})	P_3 (90% of P_{Max})	P_4 (60% of P_{Max})	P_5 (40% of P_{Max})	P_6 (30% of P_{Max})	P_7 (18% of P_{Max})	P_8 (12% of P_{Max})	P_9 (7% of P_{Max})	P_{10} (3% of P_{Max})	P_C
B-SB75											
w (µm)	4.85	7.4	20.5	34.5	49.0	50.5	85.0	111.0	148.0	194.0	51
	4.90	7.6	20.9	35.5	50.0	51.5	87.0	115.0	152.0	198.0	53
	4.89	7.68	20.7	35.18	49.95	51.75	87.1	113.3	152.2	198.2	54
Avg.	4.88	7.56	20.70	35.06	49.65	51.25	86.37	113.10	150.73	196.73	52.67
CoV	0.44	1.56	0.79	1.19	0.93	1.05	1.12	1.45	1.28	0.98	2.37
l_{FPZ} (µm)	4.7	7.5	21.0	26.0	38.5	46	34.5	22.5	17.2	12.5	47.0
	4.8	7.7	21.2	26.8	39.5	45	35.5	23.3	17.8	12.9	48.0
	4.75	7.6	21.1	26.5	39.3	46.5	35.0	22.9	17.5	12.7	47.5
Avg.	4.75	7.60	21.10	26.43	39.10	45.83	35.00	22.90	17.50	12.70	47.50
CoV	0.86	1.07	0.39	1.25	1.10	1.36	1.17	1.43	1.40	1.29	0.86
B-MB150											
w (µm)	7.5	13.5	24.3	40.32	51	60.5	92.0	116.0	150.2	220.2	69
	7.6	13.8	26.5	41.5	54	61.8	94.5	120.0	154.9	225.4	74
	7.55	13.6	27	40.04	53.5	61.13	93.34	118.1	160.2	230.5	76
Avg.	7.55	13.63	25.93	40.62	52.83	61.14	93.28	118.03	155.10	225.37	73
CoV	0.54	0.91	4.52	1.56	2.48	0.87	1.10	1.38	2.63	1.87	4.03
l_{FPZ} (µm)	9.3	29.8	50.1	70	87.0	91	77	61.5	52.5	37.5	90
	9.7	31.2	51.3	71.4	88.5	90	70.6	66.5	56.2	38	92
	9.5	30.5	50.7	69	87.5	89	75	58.8	44.3	38.34	95
Avg.	9.50	30.50	50.70	70.13	87.67	90.00	74.20	62.27	51.00	38	92.33
CoV	1.72	1.87	0.97	1.40	0.71	0.91	3.60	5.12	9.75	0.91	2.23
B-LB250											
w (µm)	9.5	15	35.2	65.0	80.2	90.0	128.0	187.0	243.0	338.0	95
	9.3	16.4	38.2	69.0	78.3	96.0	135.0	195.0	256.0	355.0	100
	9.2	18.2	40.3	67.1	83.4	92.2	132.9	192.1	250.1	346.6	98
Avg.	9.33	16.53	37.90	67.03	80.63	92.73	131.97	191.37	249.70	346.53	97.67
CoV	1.34	7.92	5.52	2.44	2.61	2.67	2.22	1.73	2.13	2.00	2.10
l_{FPZ}	24.0	27.0	39.0	75	90	110	72.0	56.0	40.0	30.0	120
	26.0	30.0	43.0	84	95	125	79.0	64.0	47.0	35.0	135
	25.1	28.5	41.0	67.6	85	110	74.0	60.0	44.0	33.4	126
Avg.	25.03	28.50	41.00	75.53	90.00	115.00	75.00	60.00	43.67	32.80	127
CoV	3.27	4.30	3.98	8.88	4.54	6.15	3.93	5.44	6.57	6.36	4.85
B-VB-500											
w (µm)	8.7	16.5	38.0	80.0	105.0	120.0	164.0	210.0	296.0	530.0	128
	9.5	18.5	41.0	90.0	115.0	135.0	185.0	245.0	318.0	570.0	145
	9.2	17.7	39.8	85.0	111.0	127.0	172.9	229.2	307.4	550.0	138
Avg.	9.13	17.57	39.60	85.00	110.33	127.33	173.97	228.07	307.13	550.00	137
CoV	3.61	4.68	3.11	4.80	3.72	4.81	4.95	6.27	2.92	2.97	5.09
l_{FPZ} (µm)	65.0	70.0	82.0	119.0	130.0	160.0	145.0	120.0	74.0	67.0	170
	73.0	80.0	89.0	125.0	140.0	180.0	160.0	145.0	92.0	75.0	172
	69.0	75.0	85.5	123.2	140.2	170.2	153.9	133.3	84.2	71.0	174
Avg.	69.00	75.00	85.50	122.40	136.73	170.07	152.97	132.77	83.40	71.00	172
CoV	4.73	5.44	3.34	2.05	3.48	4.80	4.03	7.69	8.84	4.60	0.95
B-HB-1000											
w (µm)	15	30	70	105	115	139	195	263	370	650	171
	17	34	80	120	130	154	210	270	400	662.5	175
	17.6	32.91	74.06	111.5	122	143	200.4	280	410	670.5	165
Avg.	16.53	32.30	74.69	112.17	122.33	145.33	201.80	271.00	393.33	661.00	170
CoV	6.72	5.23	5.50	5.48	5.01	4.36	3.07	2.57	4.32	1.28	2.41
l_{FPZ} (µm)	34.0	70.0	130.0	170	201.5	210	251.2	233.9	200	180	270
	37.0	80.0	140.0	160.4	205	214.1	264.9	220	205	190.2	285
	35.71	74.07	133.3	181.4	180	236	244.5	225	207.3	189.7	240
Avg.	35.57	74.69	134.43	170.60	195.50	220.03	253.53	226.30	204.10	186.63	265
CoV	3.45	5.50	3.09	5.03	5.65	5.19	3.35	2.54	1.49	2.52	7.06

Table 3: w (µm) and l_{FPZ} (mm) at P_1 to P_{10}.

Tab. 4 shows the maximum FPZ length developed in all five beams under consideration. It is observed the maximum FPZ length developed at 20%-26% of post peak load. It is observed that, when small and large beams are made from the same concrete, the fracture process zone (FPZ) significantly influences the energy dissipation characteristics in each beam.
In small beams, the FPZ is relatively large compared to the size of the uncracked ligament. This extensive FPZ leads to higher energy dissipation per unit area of crack growth due to more pronounced microcracking, aggregate interlocking, and frictional effects. Consequently, the fracture process in small beams exhibits a more ductile-like behavior, characterized by a gradual post-peak decline and a pronounced tail in the load-displacement curve.
In large beams, the FPZ is proportionally smaller relative to the beam size. The energy dissipation per unit area of crack growth is lower because the fracture behavior shifts toward a more brittle regime. Large beams typically show a steeper drop in the load-displacement curve after the peak load, reflecting reduced energy dissipation and a quicker transition to failure.

Beam ID	Iterations	P_C	l_{FPZ} (mm)
B-SB-75	1	28% of P_{Max}	47.0
	2	25% of P_{Max}	48.0
	3	24% of P_{Max}	47.5
	Avg.	26% of P_{Max}	47.50
	CoV	6.62	0.86
B-LB-150	1	20% of P_{Max}	90
	2	21% of P_{Max}	92
	3	24% of P_{Max}	95
	Avg.	22% of P_{Max}	92.33
	CoV	7.84	2.23
B-MB-250	1	21% of P_{Max}	120
	2	19% of P_{Max}	135
	3	20% of P_{Max}	126
	Avg.	20% of P_{Max}	127
	CoV	4.08	4.85
B-VB-500	1	18% of P_{Max}	170
	2	19% of P_{Max}	172
	3	22% of P_{Max}	174
	Avg.	20% of P_{Max}	172
	CoV	8.64	0.95
B-HB-1000	1	23% of P_{Max}	270
	2	19% of P_{Max}	285
	3	21% of P_{Max}	240
	Avg.	21% of P_{Max}	265
	CoV	7.78	7.06

Table 4: Maximum fracture process zone length.

Thus, small beams tend to display more ductile behavior, while large beams exhibit more brittle characteristics due to the relative influence of the FPZ on energy dissipation.

EVALUATION OF CRITICAL CRACK TIP OPENING DISPLACEMENT (w_0)

Fracture energy and tensile strength are essential parameters in the application of the bilinear softening model. This study validates the softening model parameters for the FPZ across various beam sizes. As per the cohesive crack model, the stress distribution within the FPZ of concrete is governed by the COD ($\sigma = f(w)$), with the critical crack opening displacement, w_0, being a key parameter of this relationship. Peterson's research [17] indicates that the bilinear

model is an effective representation of the stress-COD relationship. The parameters of this model include the turning point stress σ_1, w_0, w_1 and f_t.

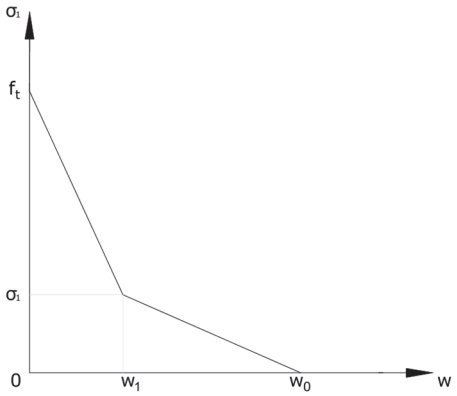

Figure 17: The bilinear softening constitutive model of concrete.

Beam ID	Iterations	Average G_f(N/m)	$\frac{G_f}{f_t}$	Pc	w_0 P7	P8	P9	P10	Average w_0 (μm)	α_n
	1	50.35	13.99	51	58.2	52.1	54	45		
	2	47.00	13.05	53	59.8	52.15	51	49		
B-SB75	3	53.15	14.76	54	59.8	48	47	48	52	3.73
	Avg.	50.17	13.93	52.67	59.27	50.75	50.67	47.33		
	CoV	5.01	5.02	2.37	1.27	3.83	5.66	3.59		
	1	83.34	23.15	69	66	68	74	80		
	2	90.12	25.03	74	74	77	73	78		
B-MB150	3	88.51	24.59	76	70	70	71	72	72.8	3.00
	Avg.	87.32	24.26	73	70	71.67	72.67	76.67		
	CoV	3.31	3.31	4.03	4.67	5.38	1.72	4.43		
	1	92.33	25.64	95	95	98	100	99.8		
	2	88.02	24.45	100	97	94	95	88		
B-LB250	3	90.67	25.19	98	85	90.6	85.4	80	93.30	3.72
	Avg.	90.34	25.09	97.67	92.33	94.20	93.47	89.27		
	CoV	1.96	1.96	2.10	5.69	3.21	6.48	9.11		
	1	146	40.56	128	136	137	101	129		
	2	122.15	33.93	145	131	132	98	125.8		
B-VB500	3	115.62	32.11	138	120.6	113.6	96.1	124	123.68	3.48
	Avg.	127.92	35.53	137	129.20	127.53	98.37	126.27		
	CoV	10.21	10.22	5.09	4.96	7.89	2.05	1.64		
	1	149	41.39	171	187.8	195	222	240		
	2	125.32	34.81	175	185.5	188.9	212	235		
B-HB1000	3	128.11	35.59	165	176	193.5	208	220	198.30	5.32
	Avg.	134.14	37.26	170.3	183.10	192.47	214.00	231.67		
	CoV	7.88	7.88	2.41	2.79	1.35	2.75	3.67		

Table 5: Evaluation of α_n.

The bilinear model is highly effective in simulating the softening properties of the concrete FPZ. Wittmann et al. [14] proposed a constitutive model for concrete softening based on this approach, observing that the ratio of σ_1 / f_t for plain concrete is typically below 0.25. Asmaro [15], through inverse analysis and mode I fracture tests on plain concrete, determined that σ_1 / f_t falls within the range of 0.4 to 0.53. Using the cohesive crack model, Huang [16] developed a numerical solution for the softening curve, concluding that σ_1 / f_t is 0.25 and w_1/w_0 is 0.4.

Petersson [17] suggested that the stress-free crack opening displacement (w_0) can be obtained by defining the cohesive stress and crack opening displacement at the kink point as f_t /3 and $0.8G_f/f_t$, respectively, where f_t represents tensile strength and G_f denotes the fracture energy of concrete. The value of G_f is calculated as the area under the load-displacement curve

obtained during three-point bending (TPB) tests. By equating the area under the softening curve to the fracture energy of concrete, w_0 can be determined.

$$w_0 = \alpha_n \frac{G_f}{f_t}$$

The parameter α_n is determined differently across various models. In Hillerborg's model [25], α_n is assigned a value of 3.5. According to the CEB-FIP model [18], α_n depends on the maximum aggregate size, taking a value of 7 for a maximum aggregate size of 16 mm and 5 for a size of 32 mm. However, an alternative version of the CEB-FIP model [19] simplifies the calculation by consistently setting α_n to 5, regardless of the maximum aggregate size.
Based on the results of the present study, the α_n values presented in Tab. 5.

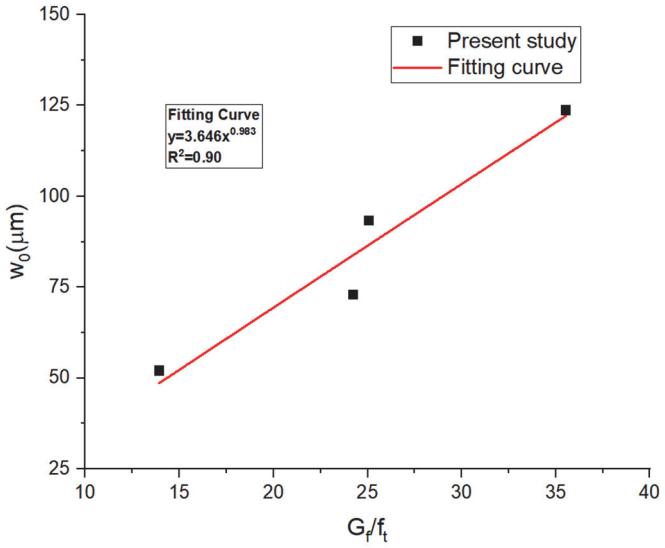

Figure 18: Relationship between the w_0 and G_f/f_t.

Fig.18 shows the relationship between the w_0 and G_f/f_t. It can be seen from the Fig.18 that, the w_0 increases with the increasement of G_f/f_t, which can be well approximated by a power function. It can be written as

$$w_0 = 3.646\left(\frac{G_f}{f_t}\right)^{0.983}$$

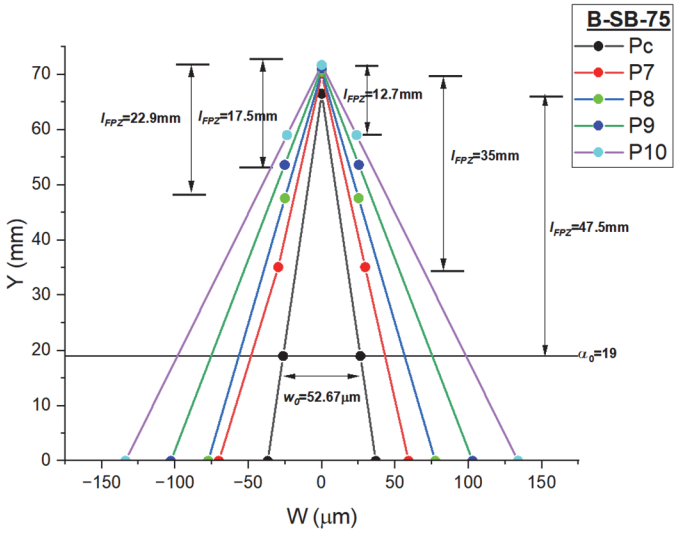

Figure 19: COD profiles of B-SB75.

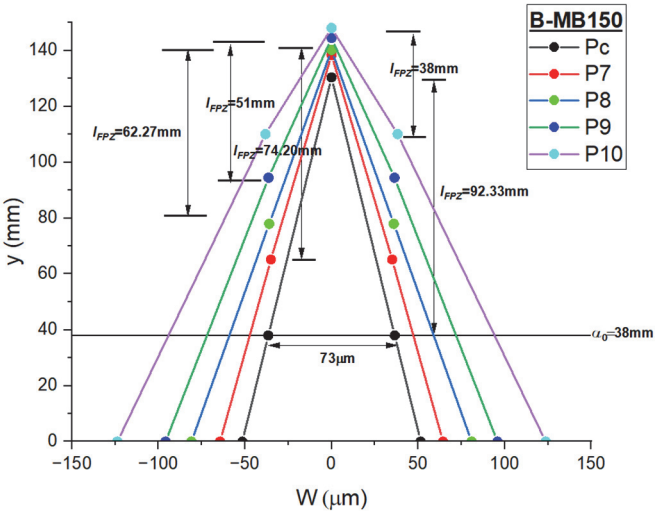

Figure 20: COD profiles of B-MB150.

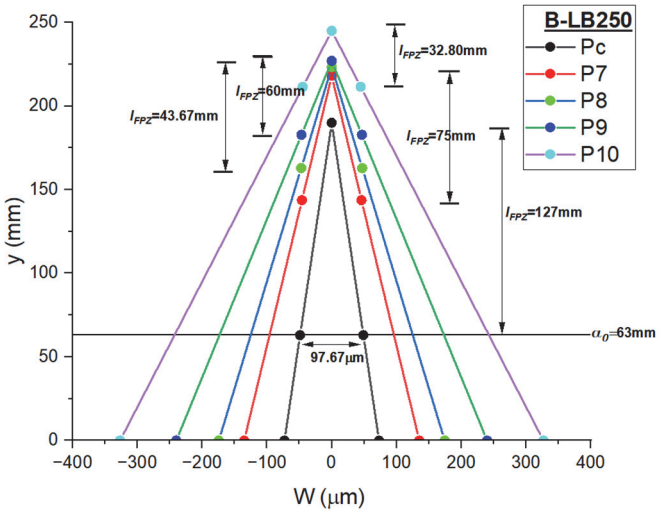

Figure 21: COD profiles of B-LB250.

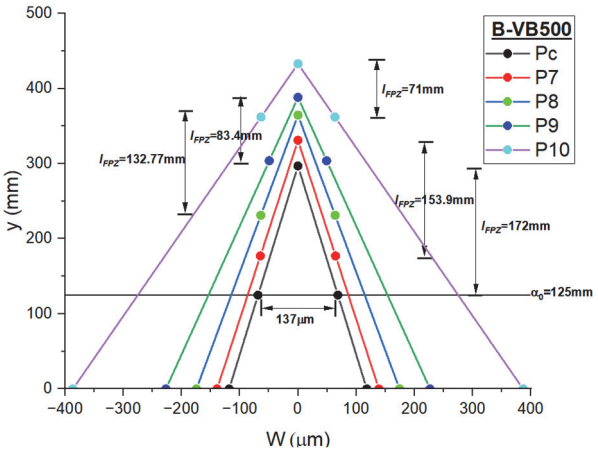

Figure 22: COD profiles of B-VB500.

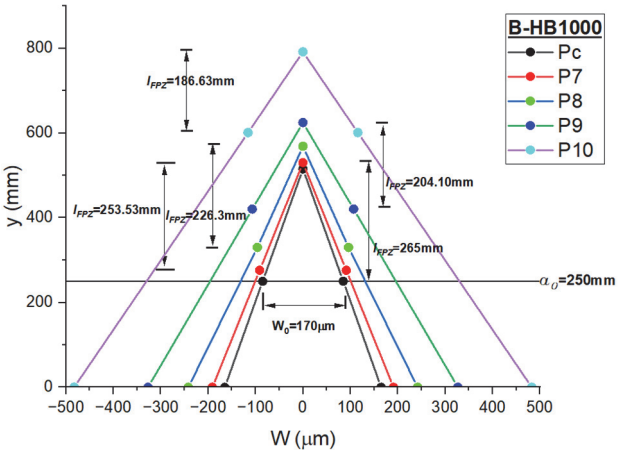

Figure 23: COD profiles of B-HB1000.

Fig.19-23 present the COD profiles of all size beams along with their corresponding FPZ lengths. It was observed that after the FPZ was fully developed, the l_{FPZ} decreased as the crack progressed. This phenomenon can be attributed to the boundary effect of the specimen, where the crack tip approached the upper boundary of the beam, leaving an insufficient remaining ligament for the further development of the FPZ.

SIZE EFFECT ON THE FPZ

As previously mentioned, the size of the FPZ ahead of the notch tip before reaching the peak load can serve as a fundamental explanation for the size effect phenomenon. Therefore, analyzing the characteristics of the FPZ across models of varying sizes holds significant importance. The current study reveals that FPZ widths are relatively consistent across all models, ranging from 3 to 5 mm. This observation aligns with findings by Skarzynski et al. [20] using the DIC technique, as well as previous numerical analyses conducted by Grassl et al. [21]. These results suggest that the FPZ width may be considered a material property.

In crack band theory, the FPZ width is generally assumed to remain constant, with Bažant [22] estimating it to be three times the maximum aggregate size. However, the FPZ widths observed in this numerical study are smaller than the assumed value. Conversely, the absolute length of the FPZ at the peak load shows a strong correlation with specimen size. Specifically, as specimen size increases, the localized damage zone lengthens, growing from approximately 47.5 mm for the smallest beam (D = 75 mm) to 265 mm for the largest beam (D = 1000 mm). This pronounced size dependence of FPZ length is attributed to the reduction in stress gradient with increasing beam size.

However, when considering the relative or normalized fracture process zone length, i.e., the ratio of FPZ length to the ligament length above the notch, $\frac{l_{FPZ}}{(D-a_0)}$, an opposite trend is observed. This ratio decreases as specimen size increases.

The present findings align with experimental observations [23, 9, 24], suggesting that the normalized FPZ length is not a material parameter but depends on model size. This size-dependent normalized FPZ length provides an intrinsic explanation for the size effect.

From Tab. 4, it is evident that l_{FPZ} for the small beam (D = 75 mm) is 47.5 mm, while for the large beam (D = 1000 mm), it is 265 mm.

$$\frac{l_{FPZ\_small}}{(D-a_0)} = \frac{47.5}{(75-19)} = 0.84$$

$$\frac{l_{FPZ\_large}}{(D-a_0)} = \frac{265}{(1000-250)} = 0.35$$

Thus the condition of $l_{FPZ\_large} < l_{FPZ\_small}$ and $\frac{l_{FPZ\_small}}{(D-a_0)} > \frac{l_{FPZ\_small}}{(D-a_0)}$ are reaffirmed.

From the crack patterns shown in Fig. 13, it is evident that the FPZ deviates due to the presence of aggregates and the weak interfacial transition zones (ITZs) around them. This suggests that the mesostructure of concrete significantly influences the formation and propagation of the FPZ.

CONCLUSIONS

1. The findings of this study align with experimental results [4, 9, 24], indicating that the normalized FPZ size is not a material property but is instead influenced by the model size. This size-dependent normalized FPZ length offers a fundamental explanation for the size effect.
2. Observations from the crack patterns reveal that the FPZ deviates due to the presence of aggregates and the associated weak ITZs, highlighting the role of concrete's mesostructure in the evolution of the FPZ.
3. The FPZ length increases initially and then decreases as the load changes. The cracks within the FPZ are narrow and regular, with the complete FPZ typically forming during the post-peak load stage.
4. The stress-free crack opening displacement (w_0) can be calculated using the expression $\alpha_n \frac{G_f}{f_t}$. In this study, α_n ranges from 3 to 3.73 for beam sizes between 75 mm and 500 mm, consistent with Hillerborg's model [31], which assigns a value of 3.5. However, for a beam size of 1000 mm, α_n increases to 5.32.
5. The FPZ length along the ligament is dependent on specimen size. Larger specimens exhibit longer regions of dissipated energy, but the increase in FPZ length is non-proportional to size.
6. In this study, $\frac{l_{FPZ\_small}}{(D-a_0)}$ is 0.84, while $\frac{l_{FPZ\_large}}{(D-a_0)}$ is 0.36, reaffirming that $l_{FPZ\_large} < l_{FPZ\_small}$ and $\frac{l_{FPZ\_small}}{(D-a_0)} > \frac{l_{FPZ\_large}}{(D-a_0)}$
7. The results provide new insights into the evolution mechanisms of the FPZ from the perspective of micro-crack initiation and propagation.

REFERENCES

[1] Abdullah, M. M., Abdulhadi, K. A. and Ali, R. R. (2019). Analysis of FPZ in concrete using DIC and ESPI techniques. Journal of Structural Engineering, 145(5), 04019040.

[2] Smith, R. A. and Jones, B. T. (2020). Investigating the fracture process zone in concrete using advanced optical techniques. Materials and Structures, 53(4), 78.

[3] Ji, Heli & Yang, Xinhua & Luo, Zuyun & Bai, Fan. (2023). Tensile Fracture Property of Concrete Affected by Interfacial Transition Zone. International Journal of Concrete Structures and Materials. 17. 2. 10.1186/s40069-022-00564-2.

[4] Vishwanatha, H. S., Muralidhara, S. and Raghu Prasad, B. K. (2023). Fracture Simulation of Concrete Beams to assess softening behavior by varying different fractions of Aggregates. Fracture and Structural Integrity, 18(67), pp. 43–57. DOI: 10.3221/IGF-ESIS.67.04

[5] Zhang, Z., Song, X., Liu, Y., Wu, D. and Song, C. (2017). Three-dimensional mesoscale modelling of concrete composites by using random walking algorithm. Composites Science and Technology, 149, pp. 235-245. DOI: 10.1016/j.compscitech.2017.06.015

[6] Trawiński, W., Tejchman, J. and Bobiński, J. (2018). A three-dimensional meso-scale modeling of concrete fracture, based on cohesive elements and X-ray CT images. Engineering Fracture Mechanics, 189, pp. 27-50. DOI: 10.1016/j.engfracmech.2017.10.003

[7] Chen, H., Xu, B., Wang, J., Nie, X. and Mo, Y. L. (2020). XFEM-based multiscale simulation on monotonic and hysteretic behavior of reinforced-concrete columns. Applied Sciences, 10(21), pp. 1-21. DOI: 10.3390/app10217899

[8] Ameli, Zahra & Rahman, Mohammod Minhajur & Carloni, Christian. (2023). Largest Experimental Investigation on Size Effect of Concrete Notched Beams. Journal of Engineering Mechanics. 150. DOI: 10.1061/JENMDT.EMENG-7225.

[9] Wu, Z. M., Rong, H., Zheng, J. J., Xu, F. and Dong, W. (2011). An experimental investigation on the FPZ properties in concrete using digital image correlation technique. Engineering Fracture Mechanics, 78, pp. 2978-2990.

[10] Muralidhara, S., Raghu Prasad, B. K., Hamid, E. and Karihaloo, B. L. (2010). "Fracture process zone size and true fracture energy of concrete using acoustic emission", Cons Build. Mater, (Elsevier Publishers) 24(4), pp. 479-486.
[11] Dai, S., Liu, X. and Kumar, N. (2019). Experimental Study on the Fracture Process Zone Characteristics in Concrete Utilizing DIC and AE Methods. Applied Sciences. 9. 1346. 10.3390/app9071346.
[12] Ren, X., Yang, W., Zhou, Y. and Li, J. (2008). Behavior of high-performance concrete under uniaxial and biaxial loading. ACI Materials Journal, 105(6), 548.
[13] Bu, J., Chen, X., Hu, L., et al. (2020). Experimental study on crack propagation of concrete under various loading rates with digital image correlation method. International Journal of Concrete Structures and Materials, 14, 25. DOI: 10.1186/s40069-020-00400-5.
[14] Wittmann, F. H., Mihashi, H. and Nomura, N. (1990). Size effect on fracture energy of concrete. Journal of Engineering Mechanics, 35(1/2/3), pp. 107-115.
[15] Asmaro, W. P. (2013). Identification of concrete fracture parameters using digital image correlation and inverse analysis. University of Windsor.
[16] Huang, C. (2016). Research on mechanical properties of concrete fracture process zone based on digital image correlation method. Chongqing: Chongqing Jiaotong University. (in Chinese).
[17] Peterson, P. E. (1981). Crack growth and development of fracture zone in plain concrete and similar materials. Report No TVBM-1006. Lund Institute of Technology.
[18] CEB-FIP model code. (1990).
[19] CEB-FIP model code. (2010).
[20] Skarżyński, Ł., Syroka, E. and Tejchman, J. (2011). Measurements and calculations of the width of the fracture process zones on the surface of notched concrete beams. Strain, 47(S1), pp. 319-332. DOI: 10.1111/j.1475-1305.2008.00605.x
[21] Grassl, P., Grégoire, D., Rojas Solano, L. and Pijaudier-Cabot, G. (2012). Meso-scale modelling of the size effect on the fracture process zone of concrete. International Journal of Solids and Structures, 49, pp. 1818-1827.
[22] Bažant, Z. P. and Oh, B. H. (1983). Crack band theory for fracture of concrete. Materials and Structures, 16(3), pp. 155-177.
[23] Muralidhara, S., Raghu Prasad, B. K. and Singh, R. K. (2013). Size independent fracture energy from fracture energy release rate in plain concrete beams. Engineering Fracture Mechanics, 98(1), pp. 284–295. DOI: 10.1016/j.engfracmech.2012.10.007.
[24] Alam, S.Y., Saliba, J. and Loukili, A. (2014). Fracture examination in concrete through combined digital image correlation and acoustic emission techniques. Construction and Building Materials, 69, pp. 232-242.
[25] Hillerborg, A., Modéer, M. and Petersson, P.-E. (1976). Analysis of crack formation and crack growth in concrete by means of fracture mechanics and finite elements. Cement and concrete research, 6(6), pp. 773-781.